Complex magnetism of Ho-Dy-Y-Gd-Tb hexagonal high-entropy alloy

J. Lužnik,[1] P. Koželj,[1] S. Vrtnik,[1] A. Jelen,[1] Z. Jagličić,[2] A. Meden,[3] M. Feuerbacher,[4,*] and J. Dolinšek[1,†]

[1]*J. Stefan Institute and University of Ljubljana, Faculty of Mathematics and Physics, Jamova 39, SI-1000 Ljubljana, Slovenia*

[2]*Institute of Mathematics, Physics and Mechanics and University of Ljubljana, Faculty of Civil and Geodetic Engineering, Jadranska 19, SI-1000 Ljubljana, Slovenia*

[3]*University of Ljubljana, Faculty of Chemistry and Chemical Technology, Večna pot 113, SI-1000 Ljubljana, Slovenia*

[4]*Institut für Mikrostrukturforschung, Forschungszentrum Jülich, D-52425 Jülich, Germany*

(Received 25 August 2015; revised manuscript received 13 November 2015; published 7 December 2015)

Rare earth based equimolar Ho-Dy-Y-Gd-Tb hexagonal high-entropy alloy (HEA) is a prototype of an ideal HEA, stabilized by the entropy of mixing at any temperature with random mixing of elements on the hexagonal close-packed lattice. In order to determine intrinsic properties of an ideal HEA characterized by the enormous chemical (substitutional) disorder on a weakly distorted simple lattice, we have performed measurements of its magnetic and electrical response and the specific heat. The results show that the Ho-Dy-Y-Gd-Tb hexagonal HEA exhibits a rich and complex magnetic field-temperature (H,T) phase diagram, as a result of competition among the periodic potential arising from the electronic band structure that favors periodic magnetic ordering, the disorder-induced local random potential that favors spin glass-type spin freezing in random directions, the Zeeman interaction with the external field that favors spin alignment along the field direction, and the thermal agitation that opposes any spin ordering. Three characteristic temperature regions were identified in the (H,T) phase diagram between room temperature and 2 K. Within the upper temperature region I (roughly between 300 and 75 K), thermal fluctuations average out the effect of local random pinning potential and the spin system behaves as a pure system of compositionally averaged spins, undergoing a thermodynamic phase transition to a long-range ordered helical antiferromagnetic state at the Néel temperature $T_N = 180$ K that is a compositional average of the Néel temperatures of pure Tb, Dy, and Ho metals. Region II (between 75 and 20 K) is an intermediate region where the long-range periodic spin order "melts" and the random ordering of spins in the local random potential starts to prevail. Within the low-temperature region III (below 20 K), the spins gradually freeze in a spin glass configuration. The spin glass phase appears to be specific to the rare earths containing hexagonal HEAs, sharing properties of site-disordered spin glasses and geometrically frustrated (site-ordered) spin systems, as a consequence of strongly interacting large abundant spins of four magnitudes (those of Gd, Tb, Dy, and Ho) on the hexagonal lattice, being weakly diluted by nonmagnetic yttrium atoms.

DOI: 10.1103/PhysRevB.92.224201 PACS number(s): 61.43.−j, 75.50.Lk

I. INTRODUCTION

High-entropy alloys (HEAs) are metallic alloys composed of multiple principal elements in equimolar or near-equimolar ratios, where a high entropy of mixing stabilizes disordered solid solution phases with simple structures, like a body-centered cubic (bcc), a face-centered cubic (fcc) [1–3], and a hexagonal close-packed (hcp) structure [4,5]. A HEA typically contains 4–9, and occasionally up to 20, elements [6]. The formation and stability of a HEA phase is determined by the Gibbs free energy of mixing $\Delta G_{\rm mix} = \Delta H_{\rm mix} - T\Delta S_{\rm mix}$, where $\Delta H_{\rm mix}$ is the mixing enthalpy and $\Delta S_{\rm mix}$ is the mixing entropy. In ideal solutions, intermolecular forces are the same between every pair of molecular kinds and there is no enthalpy of mixing $\Delta H_{\rm mix} = 0$, so the Gibbs free energy contains the entropy term only, $\Delta G_{\rm mix} = -T\Delta S_{\rm mix}$. Since $\Delta G_{\rm mix}$ is negative at any temperature, a disordered solid solution is thermodynamically stable down to zero temperature and the components are miscible in all proportions, with mixing being random. For an ideal solid solution, the mixing entropy of an r-component system is given by $\Delta S_{\rm mix} = -nR\sum_{i=1}^{r} c_i \ln c_i$, where n is the total number of moles, $c_i = n_i/n$ is the mole fraction of component i, and R is the gas constant [7]. For equimolar concentrations of elements $c_i = 1/r$, the entropy of mixing reaches its maximum value $\Delta S_{\rm mix} = nR\ln r$. In regular (nonideal) solutions, the interactions between unlike molecules are different from those between like molecules, which results in nonrandom mixing, and the mixing enthalpy is nonzero $\Delta H_{\rm mix} \neq 0$. If the elements are chosen such that $\Delta H_{\rm mix}$ is neither too high positive nor too high negative, the mixing entropy term $T\Delta S_{\rm mix}$ prevails at high temperatures and stabilizes a solid solution. This is conveniently expressed by the thermodynamic parameter $\Omega = T_m \Delta S_{\rm mix}/|\Delta H_{\rm mix}|$ [8], where $T_m = \sum c_i T_m^i$ is the compositional-average melting temperature (T_m^i is the melting temperature of component i) and $\Delta H_{\rm mix} = \sum_{i,j,i\neq j} c_i c_j H_{ij}$, where H_{ij} is the mutual mixing enthalpy of the components i and j. It is considered that for $\Omega > 1.1$, the entropy term dominates over the enthalpy and stabilizes a HEA phase, typically at temperatures higher than 1000 K. At lower temperatures, the entropy term $T\Delta S_{\rm mix}$ loses its importance and the disordered solid solution no longer represents the state of lowest energy, which is then determined by the mixing enthalpy. Positive $\Delta H_{\rm mix}$ causes incomplete miscibility and leads to phase segregation, whereas negative $\Delta H_{\rm mix}$ leads to the formation of intermetallic compounds. However, unfavorable kinetics with sluggish atomic diffusion hinders phase transformations, so the simple high-temperature structure of a disordered solid solution is retained down to low

*Corresponding author: m.feuerbacher@fz-juelich.de

†Corresponding author: jani.dolinsek@ijs.si

TABLE I. Structural properties of pure RE elements in the metallic state and the $Ho_{19.3}Dy_{19.5}Y_{20.5}Gd_{21.1}Tb_{19.6}$ HEA [15]. Theoretical lattice parameters of the HEA were calculated by Vegard's rule of mixtures.

	Y	Gd	Tb	Dy	Ho	HEA exp.	HEA theory
Structure (300 K)	hcp	hcp	hcp	hcp	hcp	hcp	
a (Å)	3.650	3.634	3.606	3.592	3.578	3.613	3.613
c (Å)	5.734	5.781	5.697	5.650	5.618	5.704	5.698
Atomic radius (Å)	1.8015	1.8013	1.7821	1.7726	1.7678		

temperatures, whereas fine crystallites of intermetallic phases or dendrites may form within the simple matrices. Mixing of the elements under the condition $\Delta H_{\mathrm{mix}} \neq 0$ is in principle nonrandom, so preferential chemical environments are formed in the crystal lattice on the scale of nearest neighbors, at least in a HEA material that has been thermally annealed just below the melting temperature. Regular HEAs at ambient temperatures thus represent an inhomogeneous state containing microstructure that cannot be reproducibly synthesized and depends on thermal history. Physical properties of such HEAs are difficult to predict theoretically (for example, the entropy of mixing can no longer be described by the simple relation $\Delta S_{\mathrm{mix}} = nR\ln r$) and the experimental data may depend on the timescale of the measurement technique. The known HEAs from the systems CuCoNiCrAlMnFeTiV [3], NbMoTaWV [9], and TaNbZrHfTi [10,11] all form bcc and fcc structures and without exception belong to the class of regular HEAs (with $\Delta H_{\mathrm{mix}} \neq 0$). The question of what are the intrinsic properties of an equilibrium homogeneous multicomponent solid solution with random mixing of the elements on a simple crystal lattice, i.e., those of an ideal HEA, thus remains unanswered.

Rare earth (RE) metals show great similarity in their chemical properties, which allows almost complete mutual solubility. Recently, a hexagonal HEA was synthesized using the RE elements Gd, Tb, Dy, Ho, and Y [4]. For these five elements, the mutual mixing enthalpies for each pair are zero $H_{ij} = 0$ [12], and so is their weighted sum $\Delta H_{\mathrm{mix}} = 0$, assuring random mixing of the elements, phase homogeneity and thermodynamic stability down to zero temperature. Pure metals possess the same hcp crystal structure with small differences in the a and c lattice parameters, originating from the known lanthanide contraction of atomic radii r_i toward heavier RE elements (Table I). Since the elements Gd, Tb, Dy, and Ho are neighbors in the periodic system, the radius-difference parameter for the equimolar Ho-Dy-Y-Gd-Tb HEA is minimized, amounting to $\delta r = \sqrt{\sum_i c_i(1 - r_i/\bar{r})^2} = 0.77\%$ (with $\bar{r}$ being the compositional-average radius), which is small compared to other known bcc and fcc HEAs, where the values of δr below 6.5% are found generally and below 3.8% are found for single-phase HEAs [13]. The very small δr value of the Ho-Dy-Y-Gd-Tb HEA assures small distortion of its hcp lattice. Furthermore, the chosen elements all possess the same 3+ valence state and their electronegativities are similar. All this suggests that the Ho-Dy-Y-Gd-Tb system may be considered a prototype of an ideal HEA, offering the opportunity to address the question on the intrinsic properties of an equilibrium HEA at any temperature. Due to great chemical similarity of the RE metals, electronic properties of RE-based HEAs can be predictably tuned with composition, but since the employed RE elements possess disparate magnetic properties, their random mixing on an almost undistorted lattice may result in unprecedented magnetic behavior. In this paper we present an experimental study of magnetism of the equimolar Ho-Dy-Y-Gd-Tb hexagonal HEA, showing that it possesses a rich and complex magnetic field–temperature (H,T) phase diagram.

II. SAMPLE CHARACTERIZATION

The Ho-Dy-Y-Gd-Tb HEA was prepared in a high-frequency levitation furnace under a 1 bar Ar atmosphere. The details of preparation of a polygrain sample and its characterization by various electron microscopy techniques can be found elsewhere [4]. Energy dispersive spectroscopy (EDS)-determined composition was $Ho_{19.3}Dy_{19.5}Y_{20.5}Gd_{21.1}Tb_{19.6}$ (in atomic percent), with about 0.5% uncertainty for each element, so the constituent elements are in equimolar concentrations. The material was found to be homogeneous; no features due to composition variation, precipitation of secondary phases, dendrite formation, etc., could be observed. The x-ray diffraction (XRD) pattern of the investigated sample is shown in Fig. 1. All peaks could be indexed to a hcp structure (space group $P6_3/mmc$) with the lattice parameters $a = 3.613(1)$ Å and $c = 5.704(2)$ Å, in good agreement with the compositional-average theoretical values $\bar{a} = 3.613$ Å and $\bar{c} = 5.698$ Å for this alloy (Table I). The compositional

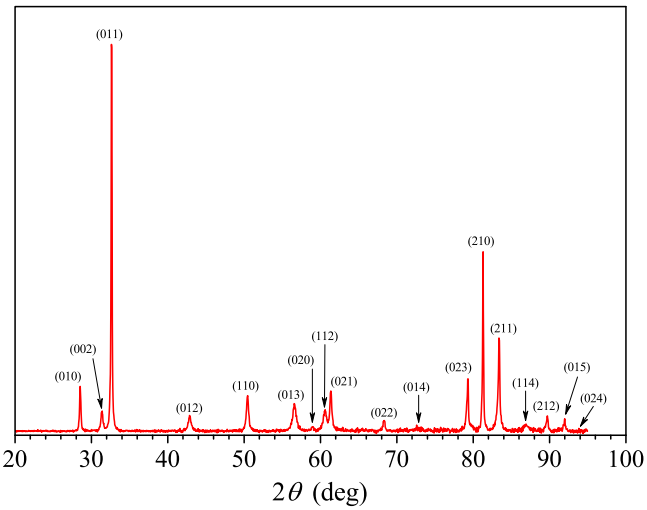

FIG. 1. (Color online) XRD pattern of the hexagonal Ho-Dy-Y-Gd-Tb HEA. The peaks are indexed to a hcp crystal lattice.

average of a given physical property $\bar{Y}$ of the mixture is calculated from the properties Y_i of constituent elements by Vegard's rule of mixtures [14], $\bar{Y} = \sum_i c_i Y_i$, which is valid for a random mixing of the elements, so the agreement between the experimental and the theoretical lattice parameters is in support of the random mixing of RE elements on the hcp lattice. In Fig. 1, Miller indices hkl of the diffraction peaks are also given in the diffraction pattern. An anisotropic broadening of the peaks could be noticed, with the $hk0$ peaks being narrower than the $00l$ peaks. This demonstrates that the structure is slightly better ordered within the hexagonal (a,b) plane than along the perpendicular c hexagonal direction. Assuming that the anisotropic peak broadening originates from the spatially anisotropic size of coherently scattering domains (within which the crystalline order is close to perfect), we obtain the mean domain dimension in the hexagonal plane about 100 nm, whereas along the hexagonal direction it is about 30 nm, thus a factor of three smaller. Another cause of the anisotropic broadening could be the anisotropic lattice strains. By making a rather unphysical assumption that the domains' size is the same in all directions and the domains are ideally large (about 1 μm in any direction), the strain (the deformation of the lattice parameter) would amount to 0.17% in the hexagonal (a,b) plane and 0.30% along the c direction. The anisotropic broadening of the XRD peaks likely originates from a combination of both effects.

III. RESULTS

Magnetic measurements were conducted by a Quantum Design Magnetic Property Measurement System (MPMS) XL-5 superconducting quantum interference (SQUID) magnetometer equipped with a 5 T magnet. In order to minimize the demagnetization effects, a needle-shaped sample was prepared and its long axis was oriented parallel to the magnetic field. Electrical resistivity and specific heat measurements were performed by a Quantum Design Physical Property Measurement System (PPMS) 9 T.

For addressing the magnetism of equimolar Ho-Dy-Y-Gd-Tb HEA, we first review the magnetic phase transitions in pure metals (Table II) [15]. Gadolinium undergoes a paramagnetic to ferromagnetic (FM) transition at the Curie temperature $T_C = 293$ K. Terbium first undergoes a transition to a helical antiferromagnetic (AFM) state at the Néel temperature $T_N = 230$ K, followed by a FM transition at $T_C = 220$ K. The same sequence is observed in dysprosium ($T_N = 179$ K, $T_C = 89$ K) and holmium ($T_N = 132$ K, $T_C = 20$ K), whereas yttrium is nonmagnetic. Magnetic properties of the triply ionized RE elements are also given in Table II.

A. Direct current magnetic susceptibility

The direct current (dc) magnetic susceptibility $\chi = M/H$ in the temperature range between 300 and 2 K in a low magnetic field $\mu_0 H = 0.8$ mT, measured for both the zero-field-cooled (zfc) and the field-cooled (fc) protocols, is shown in Fig. 2(a). At $T_N = 180$ K, a sharp singularity typical of a second-order phase transition to a long-range ordered AFM state with critical slowing of spin fluctuations is observed. The T_N of the Ho-Dy-Y-Gd-Tb HEA is practically the same as the T_N of pure dysprosium. No additional phase transition to a long-range ordered magnetic state could be detected at any other temperature, including the temperatures of the phase transitions in pure metals [in Fig. 2(a), T_Ns of pure metals are marked by dashed lines and T_Cs are marked by solid lines]. Below the AFM transition, χ_{zfc} and χ_{fc} susceptibilities start to differ (with $\chi_{zfc} < \chi_{fc}$), showing rather irregular behavior upon cooling and demonstrating that the spin system reaches different magnetic states when cooled in the absence or presence of an external magnetic field of even so small a value as 0.8 mT. At 7 K, χ_{zfc} shows a pronounced cusp. The mean effective paramagnetic moment per magnetic ion $\bar{\mu}_{\text{eff}} = \bar{p}_{\text{eff}}\mu_B$, where μ_B is the Bohr magneton and $\bar{p}_{\text{eff}}$ is the mean effective Bohr magneton number, was estimated at $T > T_N$ by assuming validity of the Curie law $\chi = C_c/T$, with C_c being the Curie constant. In that case, $\bar{p}_{\text{eff}} = \sqrt{3C_c k_B/(N_A \mu_B^2 \mu_0)}$, where N_A is the Avogadro number and μ_0 is the permeability of vacuum. To estimate $\bar{p}_{\text{eff}}$, we have replaced C_c with the experimental value of the product χT, which yielded temperature-dependent $\bar{p}_{\text{eff}}$ values amounting to $\bar{p}_{\text{eff}}(300\text{ K}) = 13.5$ and $\bar{p}_{\text{eff}}(200\text{ K}) = 21$. The theoretical $\bar{p}_{\text{eff}}$ expected from the Curie law, which assumes noninteracting localized magnetic moments, for the mixture is temperature independent and amounts to $\bar{p}_{\text{eff}} = \sqrt{\sum_i c_i p_i^2} = 8.6$, where p_is are the Bohr magneton numbers of individual elements constituting the HEA (Table II). This result shows

TABLE II. Landé g factor, angular momentum J, Bohr magneton number $p = g\sqrt{J(J+1)}$, saturated moment gJ, Néel temperature T_N, Curie temperature T_C, Debye temperature θ_D, and the electronic specific heat coefficient γ_e of the RE metals and the $Ho_{19.3}Dy_{19.5}Y_{20.5}Gd_{21.1}Tb_{19.6}$ HEA [15,17]. Theoretical values for the HEA were calculated by Vegard's rule of mixtures except for the theoretical T_N, where the averaging goes only over the Tb, Dy, and Ho.

	Y	Gd	Tb	Dy	Ho	HEA exp.	HEA theory
g		2	3/2	4/3	5/4		
J		7/2	6	15/2	8		
p		7.94	9.72	10.65	10.61		8.6
$gJ(\mu_B)$		7.0	9.0	10.0	10.0	6.7	7.1
$T_N(K)$			230	179	132	180	180.3
$T_C(K)$		293	220	89	20		
$\theta_D(K)$	248	182	176	183	190	231	196
γ_{el} (mJ/mol K^2)	8.2	6.4	4.1	9.5	6.0	∼6	6.8

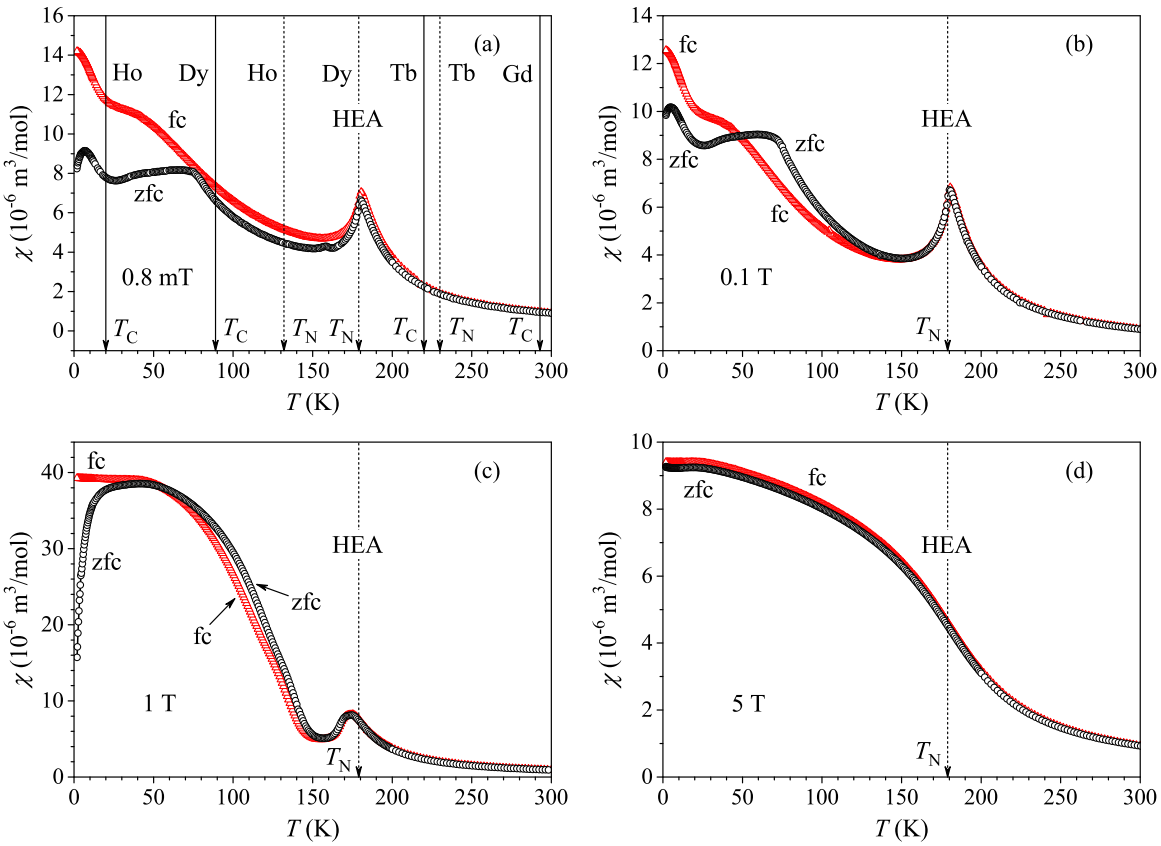

FIG. 2. (Color online) dc magnetic susceptibility $\chi = M/H$ of Ho-Dy-Y-Gd-Tb HEA in the temperature range between 300 and 2 K measured for the zfc and fc protocols in magnetic fields $\mu_0 H$ of (a) 0.8 mT, (b) 0.1 T, (c) 1 T, and (d) 5 T. In (a), the Néel temperatures T_N of pure metals and the Ho-Dy-Y-Gd-Tb HEA are marked by dashed lines, whereas the Curie temperatures T_C of pure metals are marked by solid lines. In the other three panels, only the Néel temperature of the Ho-Dy-Y-Gd-Tb HEA is marked.

that the Curie law is not applicable to the Ho-Dy-Y-Gd-Tb HEA in the paraphase within our investigated temperature range between T_N and 300 K, and the spins form short-range ordered clusters of coupled spins, which grow in size upon approaching T_N and form a long-range ordered AFM magnetic structure at T_N. The susceptibility in higher magnetic fields is shown in Figs. 2(b)–2(d). In $\mu_0 H = 0.1$ T [Fig. 2(b)], the AFM transition at $T_N = 180$ K is still well developed (not affected significantly by the external field), but below T_N, χ_{zfc} is larger than χ_{fc} down to about 50 K, where the two susceptibilities cross, so the usual situation $\chi_{zfc} < \chi_{fc}$ is observed below that temperature. In the $\mu_0 H = 1$ T field [Fig. 2(c)], the AFM transition is already significantly affected by the magnetic field. The AFM singularity is broadened and rounded and its peak position is shifted to lower temperatures, so the transition temperature in this field amounts to $T_N \approx 172$ K. Below T_N, χ_{zfc} and χ_{fc} are close to each other between T_N and about 50 K with $\chi_{zfc} > \chi_{fc}$ and both grow in a FM-like manner. At 50 K, χ_{zfc} and χ_{fc} cross, so $\chi_{zfc} < \chi_{fc}$ below that temperature and the difference $\chi_{fc} - \chi_{zfc}$ increases drastically upon further cooling. In a high field $\mu_0 H = 5$ T [Fig. 2(d)], the AFM transition is no longer observed and there is no difference between χ_{zfc} and χ_{fc}, whereas the temperature dependence of the susceptibility resembles that of a disordered ferromagnet with a field-induced FM transition smeared over a relatively large temperature interval in the region where the AFM transition takes place in low fields. The 5 T field has polarized the spins and has destroyed the magnetic structure that develops in zero or low magnetic fields.

B. Alternating current magnetic susceptibility

The response of the spin system to an alternating current (ac) magnetic field of amplitude $\mu_0 H_0 = 0.65$ mT and frequencies $\nu = 1$, 10, 100, and 1000 Hz was measured by the ac susceptibility. Its real part χ' is shown in Fig. 3(a). A sharp, frequency-independent peak is observed at $T_N = 180$ K [shown on an expanded scale in the inset of Fig. 3(a)], demonstrating a thermodynamic phase transition to an AFM state. Around 7 K, χ' exhibits a broad cusp, which is frequency dependent and shifts to higher temperatures with increasing frequency [shown on an expanded scale in Fig. 3(b)]. Such behavior is typically found in spin systems with broken ergodicity on the experimental frequency scale and indicates gradual freezing of spin fluctuations upon cooling, with a broad distribution of motional correlation times. Typical examples are spin glasses (SGs) and superparamagnets below the blocking temperature. The temperature of the cusp maximum is associated with the frequency-dependent spin freezing temperature $T_f(\nu)$ [marked by an arrow on the 1 Hz curve in Fig. 3(a)]. The $T_f(\nu)$ relation is presented in the inset of Fig. 3(b), where $T_f(\nu)$ normalized to $T_f(1\text{ Hz}) = 7.06$ K is presented. A logarithmic dependence (base 10) of T_f on

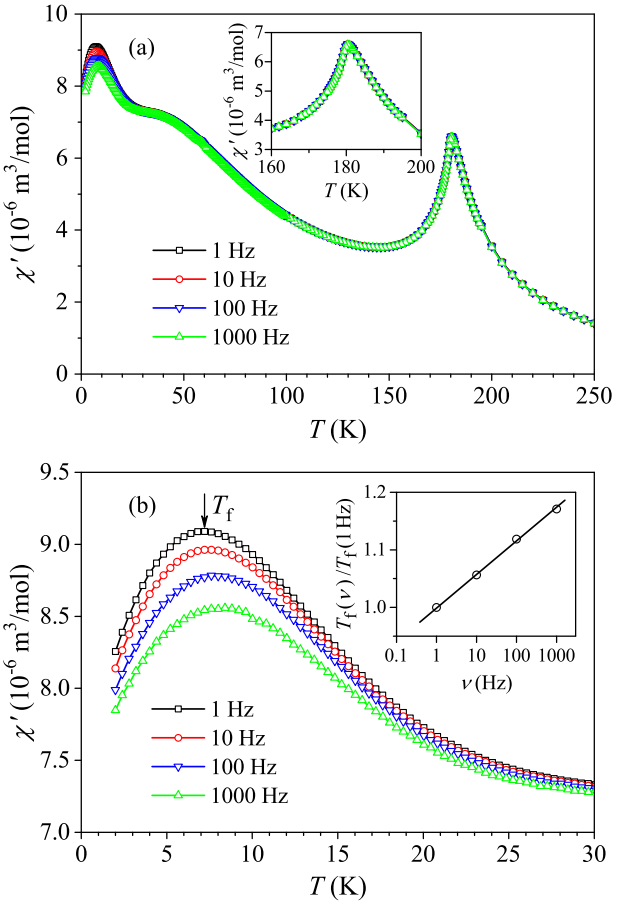

FIG. 3. (Color online) (a) Real part χ' of the ac magnetic susceptibility of Ho-Dy-Y-Gd-Tb HEA in the temperature interval between 250 and 2 K in an ac magnetic field of amplitude $\mu_0 H_0 = 0.65$ mT and frequencies $\nu = 1$, 10, 100, and 1000 Hz. The inset shows χ' on an expanded temperature scale around the AFM phase transition at $T_N = 180$ K. (b) Low-temperature χ', showing a frequency-dependent cusp around 7 K. The temperature of the cusp maximum is associated with the frequency-dependent spin freezing temperature $T_f(\nu)$ (marked by an arrow on the 1 Hz curve). The inset shows $T_f(\nu)$ normalized to the $T_f(1\text{ Hz})$ value.

the frequency is evident and the freezing temperature at the highest measured frequency of 1 kHz has increased by a factor 1.17 to a value $T_f(1\text{ kHz}) = 8.26$ K. The fractional shift of the freezing temperature per decade of frequency was evaluated to be $\Gamma = \Delta T_f / T_f \Delta(\log\nu) = 0.057$, which is a value typically found in SGs (where $\Gamma < 0.06$), whereas superparamagnets are characterized by larger values of $\Gamma \approx 0.3$ [16]. The ac susceptibility thus reveals that the phase transition at $T_N = 180$ K is a thermodynamic phase transition in an ergodic spin system, whereas the transition at 7 K is a gradual spin-freezing transition in a system with broken ergodicity.

C. Magnetization $M(H)$ curves

The magnetic state of the Ho-Dy-Y-Gd-Tb HEA was further investigated by the magnetization $M(H)$ curves measured for the magnetic field sweep of ± 5 T. The sample was always cooled in zero field to the measurement temperature, and then the field cycle was applied. The $M(H)$ curves (presented in units of Bohr magnetons per formula unit $Ho_{0.193}Dy_{0.195}Y_{0.205}Gd_{0.211}Tb_{0.196}$) for a selected set of temperatures are shown in Fig. 4. The curves change their shape qualitatively in different temperature regions and can be roughly divided into three types. The $M(H)$ curve at $T = 100$ K shown in Fig. 4(a) is typical for the upper temperature region between T_N and about 75 K (denoted as temperature region I). In the low-field regime between 0 and ± 0.65 T, the $M(H)$ relation is linear with no hysteresis, typical of an AFM state. At the field values of ± 0.65 T, the $M(H)$ curve suddenly changes its shape and becomes FM for stronger fields, also showing the FM hysteresis. Upon cycling the field between positive and negative values, this $M(H)$ shape is reversibly reproduced. The magnetic field induces a reversible AFM-to-FM spin-flop transition at a critical field value H_c, which at 100 K amounts to $\mu_0 H_c = 0.65$ T [marked by a vertical arrow in Fig. 4(a)]. Upon lowering the temperature within region I, this $M(H)$ behavior is qualitatively preserved with the following temperature-dependent behavior: the critical field H_c decreases (the spin-flop transition occurs at lower fields), whereas the width of the FM hysteresis loop increases. The temperature dependence of H_c was used to construct the temperature-magnetic field (H,T) phase diagram of Ho-Dy-Y-Gd-Tb (Fig. 5), where it is seen that within region I, $\mu_0 H_c$ drops from 1.3 T just below T_N to 0.5 T at 75 K.

The second temperature region (region II) extends roughly from 75 to 20 K. Within that region, the $M(H)$ curves show the characteristics of the curves presented in Fig. 4(b) (taken at 50 K) and Fig. 4(c) (at 25 K). The new feature is that the virgin curve (obtained when the field is applied for the first time after the zero-field cooling to the measurement temperature) is different from the curves obtained by a subsequent field cycling (the nonvirgin curves). In the 50 K curve of Fig. 4(b), it is seen that the virgin curve starts from the origin with a small slope, resembling an AFM-type curve, but grows faster after the field passes the critical field H_{c1} (which is not the same as critical field H_c of the reversible AFM-to-FM spin-flop transition in region I) and goes into saturation at high fields. After subsequent field cycling, the nonvirgin $M(H)$ curves are reversible and their shape is qualitatively the same as the shape of the curves from region I, being of the FM type except close to $H = 0$, where a tiny AFM region can still be noticed. The $M(H)$ curve on an expanded scale about the origin is shown in the inset of Fig. 4(b), where the critical fields H_c and H_{c1} are indicated by arrows (with $\mu_0 H_c = 0.3$ T and $\mu_0 H_{c1} = 0.4$ T at this temperature). The $M(H)$ at 25 K [Fig. 4(c)] again shows the difference between the virgin and the nonvirgin curves, but the FM hysteresis of the nonvirgin curve has almost vanished and the critical field H_c is zero; i.e., the helical AFM phase is no longer formed at that temperature and the nonvirgin $M(H)$ curve resembles that of a superparamagnet above the blocking temperature. These features are emphasized in the expanded portion of the $M(H)$ curve shown in the inset of Fig. 4(c). The helical AFM order and the associated field-induced AFM-to-FM spin-flop transition are thus gradually suppressed within region II upon lowering the temperature. The H_c and H_{c1} values determined from the $M(H)$ curves within region II are also presented in the (H,T) phase diagram of Fig. 5.

The low-temperature region III is entered below about 20 K, and a typical $M(H)$ curve in this region (at $T = 5$ K) is shown

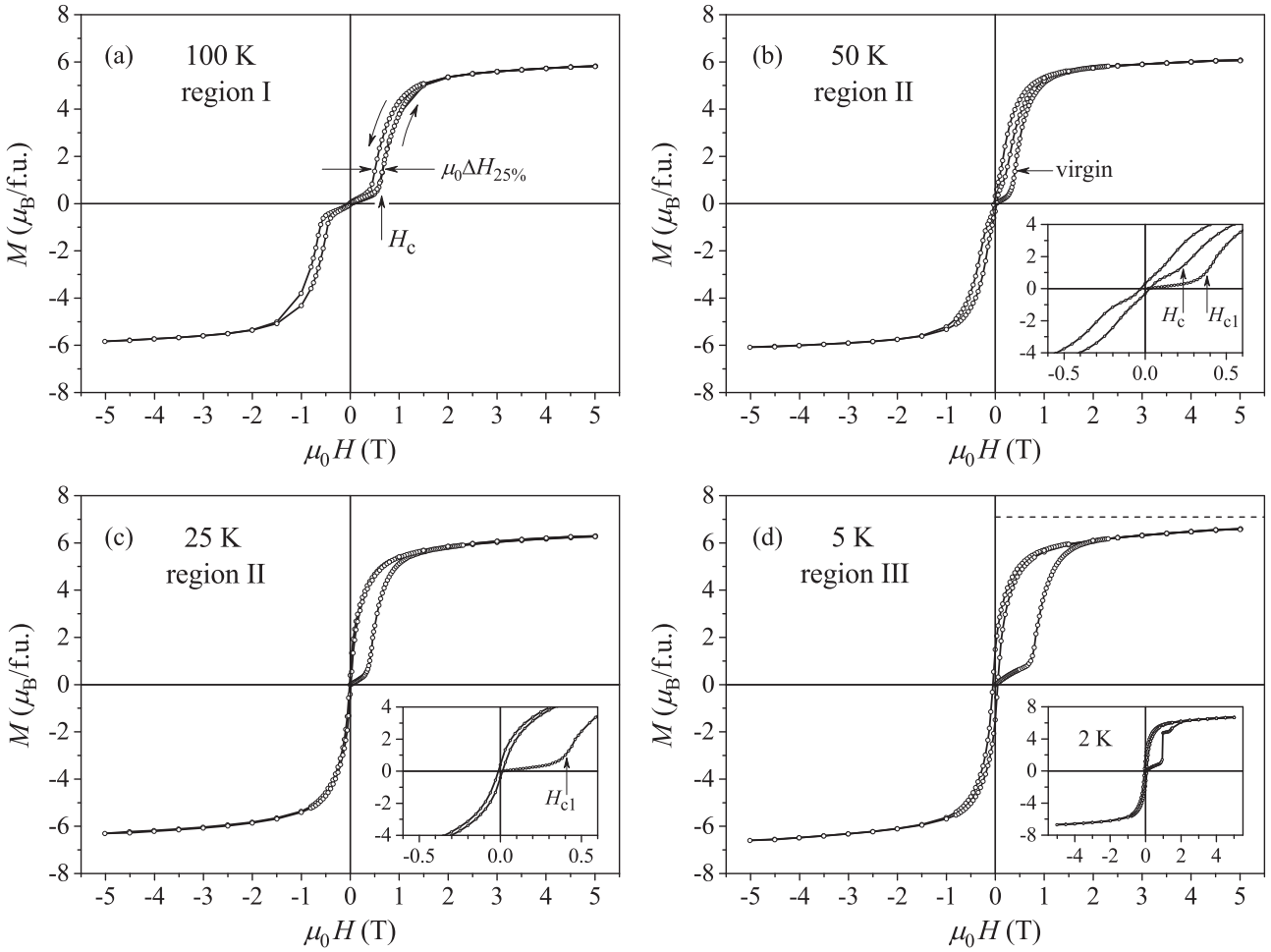

FIG. 4. Magnetization versus the magnetic field curves of the Ho-Dy-Y-Gd-Tb HEA (f.u., formula unit). (a) $M(H)$ at $T = 100$ K, typical for the upper temperature region I. The vertical arrow marks the critical field H_c of the field-induced AFM-to-FM spin-flop transition. Horizontal arrows mark the width of the FM hysteresis loop $\mu_0\Delta H_{25\%}$, taken at 25% of the saturated magnetization value. The $M(H)$ curves at (b) $T = 50$ K and (c) $T = 25$ K are typical for the intermediate temperature region II. The insets show these curves on an expanded scale about the origin, where the critical fields H_c and H_{c1} are indicated by vertical arrows. (d) The $M(H)$ curve at $T = 5$ K, typical for the low-temperature region III. The horizontal dashed line represents the theoretical compositional-average saturated magnetization $\bar{M}_s = 7.1\mu_B$, calculated by Vegard's rule of mixtures. The inset shows the $M(H)$ curve at $T = 2$ K, where the virgin curve shows a discontinuous jump at H_{c1} (indicating a kind of first-order field-induced metamagnetic transition).

in Fig. 4(d). The virgin curve exhibits small slope at low fields below H_{c1}, resembling an AFM spin order, but this is not a long-range ordered AFM state. Instead, the spins or spin domains are oriented randomly relative to each other, so the vector sum of their magnetic moments (and hence the total magnetization) is small. At H_{c1}, the virgin curve starts to grow faster with the field and reaches saturation at high fields. This behavior is similar to that of the virgin curves within region II, but the H_{c1} values within region III are considerably larger and grow strongly upon lowering the temperature. At $T = 2$ K [inset in Fig. 4(d)], the virgin curve even shows a discontinuous jump at H_{c1} (indicating a kind of first-order field-induced metamagnetic transition). The nonvirgin $M(H)$ curve is different from the virgin one and is reproducible for the repeated field cycling. Its shape resembles that of the nonvirgin curve within region II but has an important difference: the curve exhibits hysteresis, the width of which increases upon lowering the temperature (opposite to the decreasing hysteresis within region II). The physical origin of the hysteresis in the nonvirgin curves within low-temperature region III is different from the hysteresis in regions I and II. The temperature-dependent H_{c1} values within region III are also presented in the (H,T) phase diagram of Fig. 5, whereas the width of the hysteresis loops (the FM hysteresis in region I and the hysteresis width of the nonvirgin curves in regions II and III) as a function of temperature is shown in the inset of Fig. 5. All widths were determined at 25% of the saturated magnetization value [marked by horizontal arrows in Fig. 4(a)].

The experimental value of the saturated magnetization was compared to the compositional-average theoretical prediction (Table II), which can be written in the $T \to 0$ limit as $\bar{M}_s = \sum_i c_i g_i J_i \mu_B$, where g_i and J_i are the Landé factor and the total angular momentum of the element i, respectively. The theoretical value amounts to $\bar{M}_s = 7.1\,\mu_B$, whereas the experimental value read from the 5 K $M(H)$ curve at the

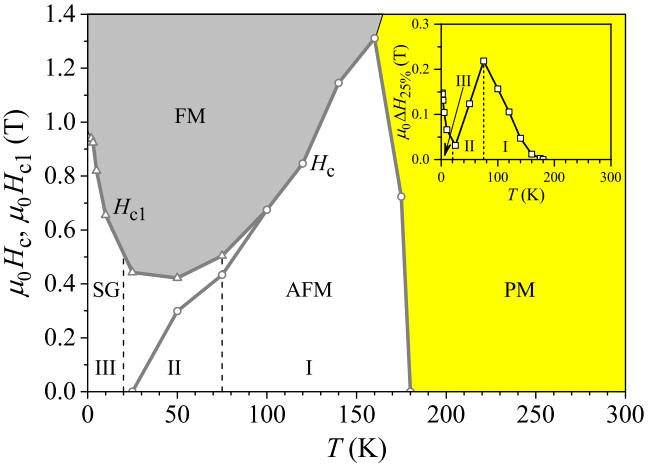

FIG. 5. (Color online) The (H,T) phase diagram of Ho-Dy-Y-Gd-Tb HEA obtained by plotting the critical fields $\mu_0 H_c$ and $\mu_0 H_{c1}$ of the $M(H)$ curves as a function of temperature. PM, paramagnetic phase. The temperature regions I–III are delimited by vertical dashed lines. The inset shows the temperature-dependent width $\mu_0 \Delta H_{25\%}$ of the $M(H)$ loops, taken at 25% of the saturated magnetization value.

highest field of 5 T amounts to $M_s = 6.7\mu_B$ [Fig. 4(d), where the theoretical $\bar{M}_s$ value is indicated by a dashed horizontal line]. Since the experimental $M(H)$ curve still grows slightly at 5 T, it is likely that the experimental M_s reaches the theoretical $\bar{M}_s$ value at higher fields, so no spins are "lost" in the total saturated magnetization and all are polarized along the field direction.

D. Specific heat

Specific heat measures the change of internal energy of the system, with temperature due to thermal excitations between its energy levels. We recall first the behavior of specific heat of pure metals [17]. Gadolinium shows a λ-type singularity at T_C, characteristic of a cooperative phase transition; terbium shows a λ singularity at T_N and a shoulder at T_C; dysprosium shows a λ singularity at T_N and a symmetric peak at T_C; and holmium shows a λ singularity at T_N and an anomaly at T_C, whereas there are no anomalies in the specific heat of the nonmagnetic yttrium. The zero-field specific heat C of Ho-Dy-Y-Gd-Tb in the temperature range between 380 and 2 K is shown in Fig. 6(a), where the temperatures of phase transitions in pure metals are also indicated (T_Ns are marked by dashed lines, and T_Cs are marked by solid lines). Ho-Dy-Y-Gd-Tb exhibits a λ-type singularity at $T_N = 180$ K, whereas no other anomaly can be observed at any temperature, including the temperatures of phase transitions in pure metals. The λ singularity in the specific heat of Ho-Dy-Y-Gd-Tb is observed at practically the same temperature as the λ singularity at T_N in pure dysprosium. The specific heat was also measured in magnetic fields up to 1 T (the use of higher fields was impractical, because the magnetic force on the sample was so large that the sample was detached from the measuring platform; the same problem occurred in the electrical resistivity measurements discussed later). The λ singularity moves with the magnetic field to lower temperatures [inset in Fig. 6(a)], where the shift of T_N in a 1 T field from the zero-field value amounts to $\Delta T_N \approx 7$ K.

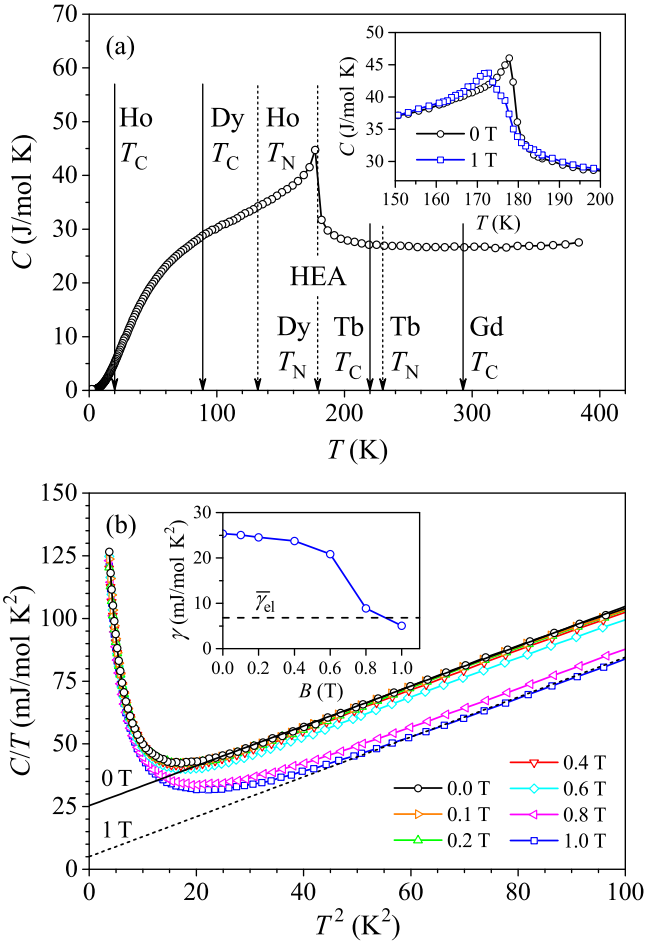

FIG. 6. (Color online) (a) Zero-field specific heat C of Ho-Dy-Y-Gd-Tb in the temperature range between 380 and 2 K. The Néel temperatures T_N of pure metals and the Ho-Dy-Y-Gd-Tb HEA are marked by dashed lines, whereas the Curie temperatures T_C of pure metals are marked by solid lines. The inset shows the λ singularity at T_N in zero magnetic field and in a 1 T field on an expanded temperature scale. (b) Low-temperature specific heat up to 10 K in magnetic fields up to 1 T shown in a C/T versus T^2 plot. Solid and dashed lines are fits of the 0 T and 1 T curves with the expression $C/T = \gamma + \beta T^2$, respectively. The inset shows magnetic field dependence of the linear coefficient γ. The dashed horizontal line represents the compositional-average electronic coefficient $\bar{\gamma}_{el}$, calculated by Vegard's rule of mixtures.

The peak is gradually rounded with a tendency to disappear. A change of slope on the high-temperature side of the peak can be noticed in the 1 T curve. Except for the field dependence of the λ singularity, no other field-induced changes can be observed in the specific heat at temperatures higher than about 20 K (the zero-field curve overlaps the curves in the field). Below 20 K, the specific heat starts to show pronounced dependence on the magnetic field. In Fig. 6(b), the low-temperature specific heat up to 10 K in magnetic fields up to 1 T is shown in a C/T versus T^2 plot. In this scale, C/T is linear except below about 4 K, where a strong upturn is observed. This upturn most likely originates from the Schottky effect [18], where the $(2J+1)$-fold degenerate energy levels of a RE ion with a total angular momentum $\hbar J$ are split by the crystalline

electric fields, which produces a broad maximum in the specific heat in the $T \to 0$ limit; here, gadolinium is an exception, because its charge cloud is spherically symmetric and the crystal-field (CF) interaction is zero. In the temperature range away from the Schottky upturn, the low-temperature specific heat was analyzed by the expression $C = \gamma T + \beta T^3$. The fit of the zero-field curve [solid line in Fig. 6(b)] has yielded the parameter values $\gamma(0) = 25\,\mathrm{mJ/mol\,K^2}$, where $\gamma(0)$ denotes the zero-field value of the linear specific heat coefficient γ, and $\beta = 7.8 \times 10^{-4}\,\mathrm{J/mol\,K^4}$. The origin of the βT^3 term can be lattice vibrations or magnetic excitations in the form of AFM magnons (or a combination of both). Within the Debye model of lattice vibrations that is usually good approximation at temperatures below 10 K, the coefficient of the cubic term β is related to the Debye temperature $\theta_D = (12\pi^4 R/5\beta)^{1/3}$, where R is the gas constant. The experimental β value has yielded $\theta_D = 231\,\mathrm{K}$. The Debye temperatures of the constituent elements are given in Table II, and their compositional average amounts to $\bar{\theta}_D = 196$ K. Because the Debye temperature is not a precisely defined quantity, the matching of the experimental θ_D value of Ho-Dy-Y-Gd-Tb to the theoretical prediction $\bar{\theta}_D$ is reasonably good, so the βT^3 term originates predominantly from the lattice vibrations; i.e., it represents the lattice contribution to the total specific heat. Magnetic excitations in the form of AFM magnons are not present in the cubic term. The linear specific heat term γT contains the electronic term $\gamma_{el} T$, where $\gamma_{el} = (\pi^2/3) k_B^2 g(\varepsilon_F)$ and $g(\varepsilon_F)$ is the electronic density of states (DOS) at the Fermi energy ε_F. The electronic specific heat coefficients of the constituent elements in their metallic state are given in Table II and their compositional average amounts to $\bar{\gamma}_{el} = 6.8\,\mathrm{mJ/mol\,K^2}$, which is much smaller than the experimental $\gamma(0)$ value. This suggests that the linear term contains another contribution. The analysis of the specific heat curves in a magnetic field presented in Fig. 6(b) reveals that this second contribution is field dependent. The curves shift downward with the increasing magnetic field, but the slopes of the linear parts of the curves do not change with the field (the curves run in parallel), so the lattice specific heat coefficient β remains unaffected. What is changing with the field is the $T = 0$ intercept of the extrapolated linear line on the vertical axis, which represents the linear specific heat coefficient γ in the C/T versus T^2 plot. The fit of the 1 T curve [dashed line in Fig. 6(b)] has yielded $\gamma(1\mathrm{T}) \approx 6\,\mathrm{mJ/mol\,K^2}$, which is close to the compositional-average electronic coefficient $\bar{\gamma}_{el}$, so the field of 1 T has already destroyed the field-dependent part of the linear coefficient γ. It is evident that the linear specific heat coefficient can be written as a sum $\gamma(H) = \gamma_{el} + A(H)$, where the electronic term γ_{el} is to a good approximation independent of the magnetic field, whereas the term $A(H)$ is field dependent and gradually vanishes in an increasing magnetic field. Such field-dependent linear contribution is found in SGs, where it is associated with the magnetic specific heat, $C_m = A(H)T$ [19]. In a SG, the interactions between spins in a magnetically frustrated configuration are distributed in strength and the spins in the ground state are frozen cooperatively in random directions. At a finite temperature T, thermal agitation causes the spins with the exchange energies of the order $k_B T$ to perform reorientations, and these low-temperature excitations contribute to the magnetic specific heat, whereas the rigidly aligned spins with stronger interactions make no contribution. Due to the distribution of interaction strengths, the spin reorientations are excited continuously over the entire SG phase upon heating, yielding a linear-in-T contribution to the magnetic specific heat. In a magnetic field, the Zeeman interaction $-\vec{\mu} \cdot \vec{B}$ "locks" the moments $\vec{\mu}$ along the field direction and impedes spin reorientations, so the magnetic specific heat at a given temperature shows a decreasing tendency for an increasing external field (spin reorientations in the field then occur at higher temperatures, where $k_B T$ is large enough to surmount both the exchange barrier and the Zeeman barrier to reorient a spin). The field dependence of the linear coefficient γ, extracted from the linear parts of the specific heat curves measured in the magnetic field, is shown in the inset of Fig. 6(b). We observe that there is first a weak field dependence in the low-field region $\mu_0 H \leqslant 0.6\,\mathrm{T}$, whereas this dependence becomes strong in higher fields. At the highest employed field of 1 T, $\gamma(H)$ has already dropped to the value of the theoretical compositional-average electronic coefficient $\bar{\gamma}_{el}$, so the field-dependent coefficient $A(H)$ has vanished in this field. The field dependence of $\gamma(H)$ closely follows the field dependence of the magnetization in region III, where the growth of the virgin magnetization curve with the magnetic field is weak below the critical field H_{c1} and strong at fields $H > H_{c1}$ [Fig. 4(d)]. From the $T < 10\,\mathrm{K}$ part of the (H,T) phase diagram shown in Fig. 5, we observe that the $\mu_0 H_{c1}$ values in region III are in the range between 0.7 and 0.9 T, which corresponds well to the field where the weak field dependence of $\gamma(H)$ turns into a strong one. The almost sudden increase of the virgin magnetization at H_{c1} is thus mirrored by the almost sudden decrease of the field-dependent (SG-type) linear specific heat coefficient $A(H)$.

E. Electrical resistivity

Electrical resistivity ρ was measured between 2 and 300 K in magnetic fields up to $\mu_0 H = 0.6\,\mathrm{T}$. The zero-field resistivity is shown in Fig. 7. The $\rho(T)$ dependence is metallic with a

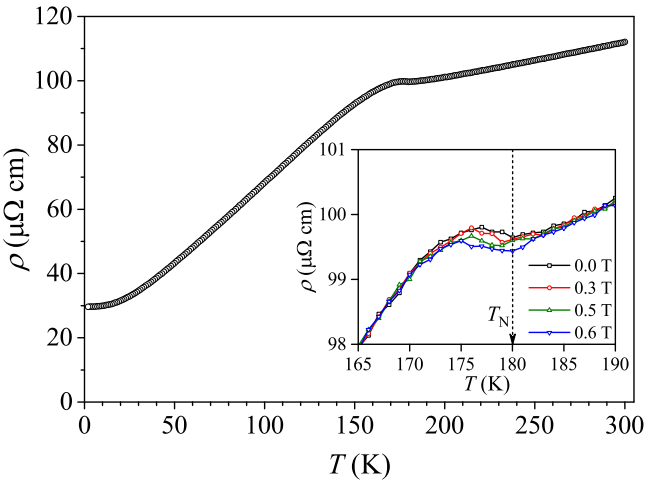

FIG. 7. (Color online) Zero-field electrical resistivity ρ of Ho-Dy-Y-Gd-Tb in the temperature interval between 2 and 300 K. The inset shows the magnetic field dependence of the resistivity in the vicinity of T_N.

positive temperature coefficient. In the $T \to 0$ limit it saturates to a residual resistivity value $\rho_{2K} = 30\,\mu\,\Omega\,\mathrm{cm}$, whereas at 300 K it amounts to $\rho_{300K} = 115\,\mu\,\Omega\,\mathrm{cm}$. A change of slope is observed around $T_N = 180\,\mathrm{K}$ and a local maximum is formed just below T_N. The maximum is field dependent and diminishes with increasing magnetic field (inset in Fig. 7). The temperature-dependent resistivity can be written as a sum of three terms: $\rho(T) = \rho_{\mathrm{imp}} + \rho_{ph}(T) + \rho_m(T)$. Here, ρ_{imp} is the residual resistivity due to elastic scattering of the electrons from impurities and from lattice defects (including lattice distortions), ρ_{ph} is the resistivity due to the inelastic electron-phonon scattering, and ρ_m originates from magnetic excitations. The ρ_m term is responsible for the field-dependent peak in the total resistivity just below T_N and originates from the "magnetic superzones" effect [20,21], as will be discussed later.

IV. DISCUSSION

A. The magnetism of pure RE metals

The key to understanding the magnetic state of the Ho-Dy-Y-Gd-Tb HEA and its (H,T) phase diagram is to consider first the magnetic behavior of its constituent elements in their metallic state. Gd, Tb, Dy, and Ho all belong to the heavy RE series, where the 4f electrons are localized. The ions possess an angular momentum $\vec{J}$ and a magnetic moment $\vec{\mu} = -g\mu_B\vec{J}$. The simplest form of Hamiltonian that adequately explains most of the magnetic structures of pure heavy RE metals is [15]

$$\mathcal{H} = \sum_i \mathcal{H}_{\mathrm{CF}}(i) - \frac{1}{2}\sum_{ij}\mathcal{J}(ij)\vec{J}_i\cdot\vec{J}_j + g\mu_B\sum_i \vec{J}_i\cdot\vec{B}, \quad (1)$$

where the summations run over all RE ions. The term $\mathcal{H}_{\mathrm{CF}}(i)$ is the CF Hamiltonian, describing the interaction of crystalline electric fields with the nonspherical charge distribution of the ith ion that lifts the degeneracy of the ionic $|JM_J\rangle$ states. For an ion at the lattice site with hexagonal point symmetry, as in the hcp structure, $\mathcal{H}_{\mathrm{CF}}(i)$ is written as [22]

$$\mathcal{H}_{\mathrm{CF}}(i) = \sum_{l=2,4,6} B_l^0 O_l^0(\vec{J}_i) + B_6^6 O_6^6(\vec{J}_i) \quad (2)$$

where B_l^m are CF parameters and $O_l^m(\vec{J})$ are Stevens operators. Here, $\mathcal{H}_{\mathrm{CF}}(i)$ is a single-ion interaction, acting independently at each ionic site i. The second term in Eq. (1) is the indirect exchange, by which pairs of ions are coupled through the intermediary of the conduction electrons. This two-ion interaction is isotropic and does not specify any orientation of the moments relative to the crystal axes. The last term is the Zeeman interaction of the moments with the external magnetic field $\vec{B}$. Magnetic structures of the heavy RE metals may be understood as a result of cooperation and competition between the oscillatory indirect exchange and the CF and magnetoelastic anisotropy forces in the strained lattice. Here, lattice strains modify CFs and all other magnetic interactions, resulting in a magnetoelastic coupling between the moments and the strain. The exchange is predominantly responsible for cooperative effects and magnetic ordering, whereas the CFs and magnetoelastic effects can be considered perturbations, introducing magnetic anisotropy whose essential role is to establish favored directions of the moments in the lattice. The terms B_l^0 $(l = 2,4,6)$ in the CF Hamiltonian introduce axial anisotropy (between the hexagonal direction and the hexagonal plane), whereas the term B_6^6 is responsible for the anisotropy within the hexagonal plane. The type of long-range magnetic order that develops at the transition from the paramagnetic to the magnetically ordered phase is determined by the exchange coupling constant $\mathcal{J}(ij)$, which is related to the shape of the Fermi surface. The Fermi surfaces of heavy RE elements (and of yttrium) are highly anisotropic and rather similar to one another in the paramagnetic phase [23]. By considering $\mathcal{J}(\vec{q})$, the Fourier transform of $\mathcal{J}(ij)$ defined via the relation $\mathcal{J}(\vec{q}) = \sum_j \mathcal{J}(ij)\exp\{-i\vec{q}\,(\vec{R}_i - \vec{R}_j)\}$ (where $\vec{R}_i$ are Bravais lattice vectors), the details of the Fermi surfaces imply that except for Gd, the quantity $\mathcal{J}(\vec{q}) - \mathcal{J}(0)$ exhibits a maximum at a nonzero wave vector $\vec{q}$, which is responsible for stabilizing periodic magnetic structures. The magnitude of the peak in $\mathcal{J}(\vec{q}) - \mathcal{J}(0)$ increases with atomic number. For our chosen elements, the peak in Gd occurs at $\vec{q} = 0$, whereas for Tb, Dy, and Ho it occurs at $\vec{q} \neq 0$, where the peak in Tb is weak, is stronger in Dy, and becomes robust in Ho [15]. The interaction of the 4f charge clouds of Tb, Dy, and Ho ions with the crystalline electric fields locks the $\vec{q}$ vector of the modulated magnetic structure along the hexagonal c axis, where the associated wavelength $\lambda = 2\pi/q$ is generally incommensurable with the crystal lattice. The positive CF parameter $B_2^0 > 0$ favors a transversely ordered phase, so in zero magnetic field, a helix is formed at the transition temperature T_N from the paramagnetic phase, where all moments in a particular atomic plane normal to the c axis are aligned but their relative orientations change from plane to plane [Fig. 8(a)] [24]. The expectation values of the moments take the form $J_{ix} = J_\perp\cos(\vec{q}\,\vec{R}_i + \varphi)$, $J_{iy} = J_\perp\sin(\vec{q}\,\vec{R}_i + \varphi)$, and $J_{iz} = 0$, where the x,y,z Cartesian axes point along the crystalline a,b,c directions. At the Néel temperature T_N, the Tb, Dy, and Ho metals thus become basal-plane antiferromagnets. The evolution of magnetic order below T_N occurs due to temperature variation of the competing magnetic interactions to which the moments are subjected. The variation of the expectation values of Stevens operators O_l^m gives rise to a pronounced temperature dependence of the anisotropy forces, including the magnetoelastic effect. Changes in the magnitude and orientation of the moments also alter the band structure of the conduction electrons, which in turn modifies the indirect exchange $\mathcal{J}(ij)$, so its Fourier transform $\mathcal{J}(\vec{q})$ changes with temperature. Because of the interaction between the local moments and the spins of the conduction electrons, the latter experience a potential with a period, which is generally different from that of the lattice and therefore generates extra energy gaps in the band structure. These magnetic superzone gaps [20,21] perturb the energy spectrum of the conduction electrons significantly. In particular, the regions of the Fermi surface responsible for the peak in $\mathcal{J}(\vec{q})$ are severely modified. The result is that both the position of the peak and its magnitude are reduced, thus tending to eliminate the characteristics of the exchange

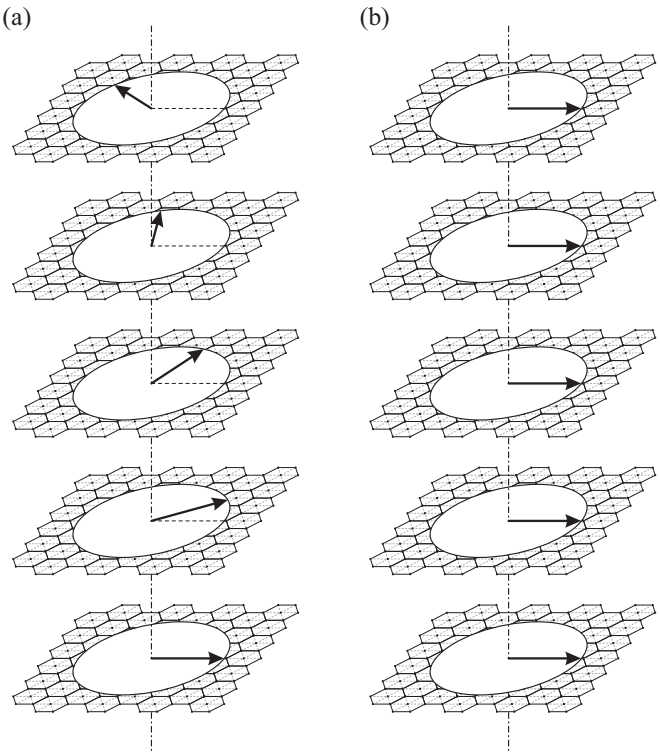

FIG. 8. Schematic representation of (a) basal-plane helical AFM structure in heavy RE metals and (b) basal-plane FM structure.

coupling that has favored a helical magnetic structure at T_N. Different temperature variations of the competing magnetic interactions impose the following evolution of the magnetic structures in Tb, Dy, and Ho metals: immediately below T_N, the exchange dominates and the anisotropy forces are small. As the temperature is lowered, the peak in $\mathcal{J}(\vec{q})$ decreases and moves toward $\vec{q} \to 0$, whereas the anisotropy forces increase. The hexagonal anisotropy B_6^6 tends to distort the helical structure by deflecting the moments toward the nearest easy axis in the hexagonal plane. The magnetoelastic forces increase until the magnetoelastic energy plus a minor contribution from the CF anisotropy just balances the difference in the exchange energy between the helical and the FM ($\vec{q} = 0$) phases. At the temperature T_C where the balance is reached, the transition to the FM phase takes place and Tb, Dy, and Ho become basal-plane ferromagnets [Fig. 8(b)]. The magnetoelastic forces thus drive the low-temperature FM transition.

The situation is different for Gd, which possesses a spherically symmetric $4f$ charge cloud and for which the CF interaction is consequently zero. A small magnetic anisotropy is still provided by the magnetic dipole interaction between the Gd moments, which locks the moments along c at $\vec{q} = 0$; i.e., a FM phase is directly formed at the transition temperature $T_C = 293$ K from the paramagnetic phase. At lower temperatures, the easy axis of magnetization begins to deviate toward the basal plane, reaching a maximum tilt angle of 60° at 180 K before decreasing to just below 30° at 4.2 K [25].

The application of an external magnetic field has a profound effect on the magnetic structures of RE metals. In a sufficiently large field, the stable magnetic configuration is an array of moments $g\mu_B J$ pointing along the field direction. The intermediate states between the zero-field structure and the high-field limit may be complex, so the (H,T) phase diagram may include field-induced continuous and/or discontinuous phase transitions to exotic metamagnetic structures (e.g., a conical structure, a multiple-$\vec{q}$ structure, a spin-slip structure, and a helifan structure). The magnetic field also eliminates the magnetic superzone gaps, because it destroys their origin—the periodic magnetic structures with periodicity different from that of the crystal lattice.

B. Magnetic ordering in the Ho-Dy-Y-Gd-Tb HEA

We turn now to the analysis of magnetic ordering and its evolution with temperature and magnetic field in the Ho-Dy-Y-Gd-Tb HEA. The XRD pattern shown in Fig. 1 demonstrates that the crystal lattice of hexagonal symmetry is well developed. Random mixing of elements on the lattice is supported by the lattice parameters and other physical parameters given in Table II obeying Vegard's rule of mixtures reasonably well. Paramagnetic moments of the ions are markedly different and amount to (in units of Bohr magneton per ion) $\mu^{Gd} = 7.94$, $\mu^{Tb} = 9.72$, $\mu^{Dy} = 10.65$, $\mu^{Ho} = 10.61$, and $\mu^{Y} = 0$ (Table II). The Ho-Dy-Y-Gd-Tb HEA thus represents a magnetic system where sizable magnetic moments of four magnitudes in equal concentrations are randomly distributed over the sites of a weakly distorted hexagonal lattice and are diluted with nonmagnetic yttrium ions. To describe such a system theoretically, a disordered variant of the Hamiltonian of Eq. (1) should be constructed and solved, which is a highly demanding task. A qualitative analysis can still be made by considering the influence of random substitutional disorder and lattice distortions on the individual terms in the Hamiltonian.

We begin with the single-ion CF term of Eq. (2). For simplicity, we perform the discussion within the point-charge model [26], where the CF parameters B_l^m are proportional to the coefficients $\gamma_{lm} = \sum_j (4\pi/2l+1) q_j [Z_{lm}(\theta_j,\phi_j)/R_j^{l+1}]$, where q_j and (R_j,θ_j,ϕ_j) are the charge and the polar coordinates of the jth ion with respect to the central RE ion, for which the interaction with the crystalline electric fields of its neighbors is calculated. The $Z_{lm}(\theta,\phi)$ are tesseral (real) harmonics (electrical multipoles), where $Z_{l0}(l = 2,4,6)$ depend on even powers of $\cos\theta$, whereas $Z_{66} \propto \sin^6\theta\cos 6\phi$. For the hcp lattice, the first coordination shell of each lattice site contains 12 atoms. All five elements constituting the HEA are in a 3+ ionization state, so the ionic charges q_j are the same regardless of the distribution of elements within the first coordination shell. Differences in the atomic radii of the five elements introduce random lattice distortions, characterized by a random distribution of the distances R_j and the polar and azimuthal angles θ_j and ϕ_j, which introduce variation of the CF parameters over the lattice sites i. Since the atomic radii differences are small, the lattice distortions are also small, as is the associated distribution of the CF parameters. The CF Hamiltonian of the Ho-Dy-Y-Gd-Tb HEA is thus not expected to change much with respect to the pure Tb, Dy, and Ho metals. At the Gd and Y sites, the CF interaction is zero. Since the five elements are in equimolar concentrations, 60% of the lattice sites (those populated by Tb, Dy, and Ho) experience the CF

interaction, whereas the remaining 40% sites (populated by Gd and Y) are insensitive to it.

Random substitutional disorder and lattice distortions modify the exchange Hamiltonian significantly. Since four types of ions with angular momenta $\vec{J}_m$ (with $m = 1-4$ referring to Gd, Tb, Dy, and Ho) are randomly distributed over the lattice sites i and diluted with nonmagnetic Y, the product $\vec{J}_i \cdot \vec{J}_j$ in the exchange Hamiltonian is replaced with terms of the form $c_{i,m}c_{j,n}(g_m - 1)(g_n - 1)\vec{J}_{mi} \cdot \vec{J}_{nj}$ (following from the Heisenberg exchange Hamiltonian being transformed from spin variables $\vec{S}$ to the total angular momentum $\vec{J}$ by a transformation $\vec{S} = (g-1)\vec{J}$ and $c_{i,m}$ being the probability that the site i is populated by an ion of the type m. The exchange coupling constant $\mathcal{J}(ij)$ also becomes distributed. It is reasonable to assume that this distribution can be described by a continuous distribution function $P(\mathcal{J}(ij))$, which is peaked at a mean value $\bar{\mathcal{J}}(ij)$ and has a width $\Delta\mathcal{J}(ij)$, so the exchange interaction in the Ho-Dy-Y-Gd-Tb HEA becomes a random-bond problem. The Zeeman interaction is also modified by the disorder. The magnetic field $\vec{B}_i$ acting on the spin at the site i becomes a random variable, being a sum of the external field $\vec{B}$ and the local molecular field that includes the dipolar field of its neighbors. The Hamiltonian of the substitutionally disordered spin system with the exchange coupling constant described by a distribution $P(\mathcal{J}(ij))$, and the random field variable $\vec{B}_i$ is thus a random-bond, random-field problem, analogous to the Sherrington-Kirkpatrick model [27] used to describe SGs.

The main effect of the disorder is an additional potential experienced by the spins. This potential varies randomly over the lattice sites and provides local pinning centers for the spin orientations. At high temperatures, the thermal energy k_BT is large enough to overcome this potential and the thermally fluctuating spin system acts as an ergodic system whose properties are predominantly determined by the average value of the exchange coupling constant $\bar{\mathcal{J}}(ij)$, whereas the time-average molecular field is negligible (so that $\vec{B}_i \approx \vec{B}$). The CF Hamiltonian is also not affected much by the disorder. Under these conditions the magnetic state of the HEA can be described within the virtual crystal approximation (VCA) [15], where the angular momentum at each lattice site is replaced with a compositional average $\vec{J}_{av} = (1/5)\sum_{m=1}^{5}\vec{J}_m$ (here the sum runs over all five elements constituting the HEA with the constraint that the angular momentum of Y is zero), interacting with its neighbors via the average exchange coupling $\bar{\mathcal{J}}(ij)$ and experiencing the external magnetic field $\vec{B}$. The parameters of the CF Hamiltonian can also be taken as the compositional average (where $\mathcal{H}_{\mathrm{CF}}$ of Gd and Y is zero). In the VCA, the disorder-induced pinning potential is neglected due to fast thermal fluctuations of the spins and the spin system behaves as a pure system of compositionally averaged spins coupled via the exchange and interacting with the crystalline electric fields and external magnetic field that assume sharp (nondistributed) values. The VCA can be applied to the Ho-Dy-Y-Gd-Tb HEA within region I in the (H,T) phase diagram of Fig. 5, where the sharp peak in the dc and ac magnetic susceptibilities and the λ-type singularity in the specific heat in zero and low magnetic fields demonstrate the transition to the AFM state at the Néel temperature $T_N = 180$ K. The T_N of the Ho-Dy-Y-Gd-Tb HEA coincides with the compositional average of the Néel temperatures of Tb, Dy, and Ho metals $\bar{T}_N = (T_N^{Tb} + T_N^{Dy} + T_N^{Ho})/3 = 180.3$ K (Table II), which is accidentally almost equal to the Néel temperature of pure dysprosium ($T_N^{Dy} = 179$ K). Details of the AFM structure that develops at T_N cannot be directly inferred from our experiments (this can be done, e.g., by magnetic neutron scattering), but the electrical resistivity that shows the magnetic superzone effect just below T_N supports the hypothesis that the magnetic structure is periodic, with a periodicity different from that of the lattice. Since the CF parameters B_2^0 of Tb, Dy, and Ho are all positive [15] (where $B_2^0 > 0$ favors a transversely ordered phase), it is reasonable to consider that the zero-field magnetic structure of the Ho-Dy-Y-Gd-Tb HEA within the high-temperature region I is a basal-plane helical antiferromagnet, analogous to the same type of magnetic ordering in the Tb, Dy, and Ho metals. These three elements predominantly determine the magnetic structure of the Ho-Dy-Y-Gd-Tb HEA within region I, whereas the influence of Gd (with no CF interaction) and nonmagnetic Y appears to be minor. The AFM phase transition occurs at the Néel temperature $\bar{T}_N$ that is a compositional average of T_Ns of Tb, Dy, and Ho, which suggests that the Fermi surface of Ho-Dy-Y-Gd-Tb HEA, which determines the exchange constant $\bar{\mathcal{J}}(ij)$, in region I is to a good approximation also an average of the Fermi surfaces of these elements (or, more likely, of all five constituting elements, since their Fermi surfaces in the paramagnetic phase are alike). The temperature dependence of $\bar{\mathcal{J}}(\vec{q})$, the Fourier transform of $\bar{\mathcal{J}}(ij)$, in region I can be inferred from the temperature dependence of the critical field H_c in the (H,T) phase diagram (Fig. 5). At H_c, the external magnetic field induces an AFM-to-FM spin-flop transition, so an array of spins parallel to the field is energetically preferred with respect to the helical AFM spin order. At the spin-flop transition, the Zeeman interaction just balances the exchange energy difference between the helical AFM and the field-induced FM states. The H_c decreases strongly with decreasing temperature within region I, which can be explained by considering that $\bar{\mathcal{J}}(\vec{q})$ changes with temperature in a way that the height of the maximum in $\bar{\mathcal{J}}(\vec{q}) - \bar{\mathcal{J}}(0)$ responsible for stabilizing the helical AFM state is reduced upon lowering the temperature and its position shifts toward $\vec{q} \to 0$. The energetic stability of the helical AFM state is thus reduced upon lowering the temperature in the same way as in the pure Tb, Dy, and Ho metals. These three metals undergo in zero field a transition from the basal-plane helical AFM state to a basal-plane FM state, but in the Ho-Dy-Y-Gd-Tb such a transition never occurs because at lower temperatures, the thermal energy is no longer sufficient to average out the effect of the disorder-induced random pinning potential. Upon cooling, the pinning potential starts to increasingly affect the magnetic state of the Ho-Dy-Y-Gd-Tb HEA, which is manifested by the appearance of the zfc-fc susceptibility splitting in low magnetic fields (Fig. 2). Within region I, the effect of the random pinning potential is still small.

In the temperature region II, extending roughly between 75 and 20 K, the decreasing periodic potential responsible for the formation of the helical AFM state and the random pinning potential become of comparable strength and compete with each other. This is best manifested in the $M(H)$ curves of Fig. 4(b) and (c), where the virgin curve is different from the curves obtained by subsequent field cycling. This indicates that the free energy of the spin system contains several degenerate or nearly degenerate minima separated by barriers that can be surmounted only by a sufficiently high thermal energy k_BT or the application of an external magnetic field $\vec{B}$. In the low-field region between zero and the critical field H_{c1}, the virgin magnetization is small and its growth with the field is weak, so the spins freeze in random directions in the random local fields when cooled in the absence of an external magnetic field. At fields higher than H_{c1}, the Zeeman interaction of spins with the external magnetic field wins over the interaction with the random molecular fields and favors spin alignment along the field direction. Due to the degeneracy of the free energy landscape, the state of the spin system achieved during cooling in zero field is not retrieved after the field application. The subsequent evolution of spin order upon the magnetic field cycling approaches that of a superparamagnet, as evidenced from the vanishing tendency of the hysteresis loop width on cooling within region II (inset in Fig. 5). This indicates that the helical AFM spin order created by the periodic potential is gradually destroyed and the random pinning potential starts to dominate with a tendency to freeze the spins in random directions. Region II can be considered an intermediate region where the long-range periodic spin order "melts" and the random ordering of spins in the random local potential starts to prevail.

Within region III that extends below about 20 K, the magnetic state of the Ho-Dy-Y-Gd-Tb HEA is determined predominantly by the random local pinning potential that impedes thermally assisted spin reorientations so that in zero external field the spins freeze in random directions in the $T \to 0$ limit. This is schematically shown in Fig. 9, where four kinds of spins diluted with nonmagnetic Y are frozen in a SG configuration within one hexagonal layer of a hcp lattice. Since this potential is distributed in strength over the lattice sites, the spins freeze gradually upon cooling, which is evidenced from the frequency-dependent freezing temperature $T_f(\nu)$ observed in the ac susceptibility and the linear-in-T magnetic specific heat. The spin system in the Ho-Dy-Y-Gd-Tb HEA thus undergoes a gradual spin-freezing transition to a nonergodic state, where the spectrum of correlation times for spin reorientations is broad, extending from short times up to macroscopic times that are much longer than the frequency observation window of any experimental measurement technique. Such spin freezing is observed in SGs and superparamagnets below the freezing (blocking) temperature, where the two kinds of systems are usually difficult to distinguish experimentally [19]. While spin freezing in SGs is a collective phenomenon in a system of exchange-coupled spins, the spins or spin clusters in superparamagnets are uncoupled and their orientations with respect to the crystal lattice are determined by the magnetic anisotropy energy provided by the single-ion CF interaction and by the magnetic dipolar interaction. The value of the fractional shift of freezing temperature per decade of frequency $\Gamma = 0.057$ determined from the ac susceptibility of Ho-Dy-Y-Gd-Tb HEA is in the range found for SGs (for superparamagnets, the Γ values are typically one order of magnitude larger) [16], which is a hint that the broken-ergodicity state formed below $T_f \approx 7$ K in the zero external magnetic field is a collective SG state. The critical field H_{c1} (where the randomly frozen spins start to rotate into the external field direction) and the $M(H)$ hysteresis increase strongly upon lowering the temperature below 20 K, which suggests that effective interspin interactions strengthen on cooling (as a result of a decreasing thermal energy k_BT that opposes the exchange interaction), also in favor of a collective SG state. However, the discontinuous field-induced metamagnetic transition to an unidentified state observed at $\mu_0 H_{c1} = 0.93$ T in the virgin $M(H)$ curve at $T = 2$ K [inset in Fig. 4(d)] demonstrates that the magnetic structure in an external field is more complicated than for a canonical SG. Such a transition is a result of competing interspin interactions and the Zeeman interaction, which is again in favor of a collective SG state. It is thus reasonable to assume that the low-temperature broken-ergodicity magnetic state of the Ho-Dy-Y-Gd-Tb HEA formed in zero field is a SG state. In the following, we consider whether the properties of this state are similar to other known SG systems or whether it represents a new, unconventional type of SG state specific to HEA systems.

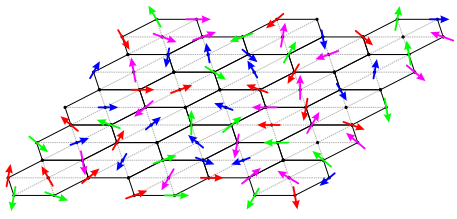

FIG. 9. (Color online) Schematic representation of low-temperature SG order within one hexagonal layer of the hcp lattice of Ho-Dy-Y-Gd-Tb HEA. Magnetic moments of Gd, Tb, Dy, and Ho ions are drawn by arrows of different colors, and the length of the arrow is proportional to the size of the moment. Nonmagnetic Y ions are presented by black dots. All five elements are in equimolar concentrations.

According to the standard definition, [19] a SG is characterized by two fundamental properties: (1) frustration (the interaction between spins is such that no configuration can simultaneously satisfy all bonds and minimize the energy at the same time) and (2) randomness (the spins are positioned randomly in the sample). The spin systems involving frustration and randomness are known as "site-disordered" SGs, and their prototypes are canonical SGs: dilute magnetic alloys of a noble metal host (Cu, Ag, Au) and a magnetic impurity (Fe, Mn). In canonical SGs, the interaction between spins is the conduction electrons mediated Ruderman-Kittel-Kasuya-Yosida (RKKY) indirect exchange interaction. This interaction oscillates in space and can be either FM or AFM, depending on the distance between the spins. Combined with randomness, the RKKY interaction results in frustration. Frustration and randomness lead to a highly degenerate free-energy landscape with a distribution of barriers between metastable states, resulting in broken ergodicity below the frequency-dependent

spin freezing temperature $T_f(\nu)$ [28]. The SG phases with similar broken-ergodicity properties also develop in pure (i.e., site-ordered) systems without quenched disorder. These are geometrically frustrated antiferromagnets with kagomé and pyrochlore lattices, where triangular or tetrahedral distribution of nearest-neighbor AFM-coupled spins frustrates an ordered periodic system [29–32]. These systems are known as "topological" or "geometrically-frustrated" SGs and again exhibit a spin-freezing transition at $T_f(\nu)$. The Ho-Dy-Y-Gd-Tb HEA contains both randomness and frustration, and the interaction between the spins is the RKKY indirect exchange. While in a canonical SG the spins are diluted in a nonmagnetic matrix, the situation is opposite in the Ho-Dy-Y-Gd-Tb, where the spins are abundant and only weakly diluted with nonmagnetic Y (Fig. 9). Randomness there occurs due to random distribution of four kinds of spins over the lattice sites and their dilution by the Y ions. Each spin in the Ho-Dy-Y-Gd-Tb HEA thus faces many nearest-neighbor spins with which it interacts strongly due to their proximity in space. Random distribution of spins within the first coordination sphere of each ion introduces a distribution of the exchange coupling constants over the lattice sites, which results in frustration of the bonds due to the site-disorder effect. Since in a hcp lattice the spins are positioned on triangles, the triangular distribution adds a geometric frustration. The SG phase in the Ho-Dy-Y-Gd-Tb HEA thus shares properties of both the site-disordered and the geometrically frustrated site-ordered systems. Due to high abundance of large spins on the lattice, the interspin interactions are considerably stronger than in the spin-diluted canonical SGs. In combination with the thermal energy that opposes spin ordering, this results in a rich variety of collective magnetic states in the (H,T) phase diagram. Due to the enormous chemical (substitutional) disorder, a theoretical description of such a system remains a challenge.

V. CONCLUSIONS

The preceding experimental results and discussion can be summarized as follows:

(1) Our paper presents the determination of intrinsic physical properties of a HEA, a consequence of classifying the investigated hexagonal Ho-Dy-Y-Gd-Tb as an ideal HEA. The ideality arises from the mutual mixing enthalpies of any pair of the employed RE elements being zero, so mixing of five elements on the lattice is random and the phase is homogeneous and thermodynamically stable down to zero temperature. All other known HEAs (composed exclusively of transition elements and forming bcc and fcc lattices) belong to the class of real HEAs, where the nonzero mixing enthalpies of the elements cause nonrandom mixing, which results in the formation of precipitates of intermetallic phases and dendrites (phase segregation). Physical properties of such highly inhomogeneous and metastable systems are not the intrinsic properties of a HEA.

(2) While investigations of HEAs with bcc and fcc structures are numerous [3], hexagonal HEAs were discovered only in 2014. Existing papers [4,5] report synthesis and characterization by electron microscopy but no physical, chemical, or mechanical properties. Our paper presents the investigation of physical properties of a hexagonal HEA.

(3) The Ho-Dy-Y-Gd-Tb HEA is characterized by an almost undistorted hcp lattice with an enormous chemical (substitutional) disorder. The system can be called "metallic glass on an ordered lattice," possessing the properties of amorphous metallic glasses and ordered crystals at the same time. Physical properties of such a dual system represent a new challenge in solid state physics, both theoretical and experimental. Our results show that the properties are unprecedented and highly nontrivial. A magnetic field-temperature phase diagram contains both long-range ordered periodic magnetic structures as expected for an ordered system and SG-type disordered structure as expected for a random system. The external magnetic field induces additional magnetic phase transitions in various temperature ranges, some continuous and others discontinuous. There is a question as to how to explain such richness of magnetic phases by a single model. In view of the enormous substitutional disorder on an ordered lattice, involving five randomly distributed chemical elements, construction of an appropriate Hamiltonian seems to be an extreme challenge. Thinking in terms of different SG-type models (e.g., a canonical SG or a cluster-glass blocking model) is oversimplified, as it cannot give a transition from a long-range ordered periodic magnetic structure to a SG-type random structure. The best one can do is to present carefully conducted experiments, hoping that theorists will gain enough experimental information to start constructing the Hamiltonian that will reproduce most of the experimental findings (and especially the aforementioned transition from the long-range periodic magnetic order to a SG-type disorder).

(4) The investigated hexagonal Ho-Dy-Y-Gd-Tb HEA exhibits a rich and complex (H,T) phase diagram as a result of competition among the periodic potential arising from the electronic band structure that favors periodic magnetic ordering, the disorder-induced local random potential that favors SG-type spin freezing in random directions, the Zeeman interaction with the external field that favors spin alignment along the field direction, and the thermal agitation that opposes any spin ordering. Though the Ho-Dy-Y-Gd-Tb HEA is the only investigated hexagonal RE-based HEA, it is likely that the specific SG phase found in this alloy at low temperatures is common to the class of hexagonal RE-based HEAs, occurring due to strongly interacting abundant spins of different magnitudes, positioned randomly on triangles in the hcp lattice, where frustration of the interspin interactions occurs from both the substitutional disorder and the geometrical effect. Here, it is essential that the Ho-Dy-Y-Gd-Tb HEA belongs to the class of ideal HEAs ($\Delta H_{\mathrm{mix}} = 0$), which assures random mixing of the elements on the lattice, so the condition of randomness for the creation of a SG phase is fulfilled. In real HEAs with $\Delta H_{\mathrm{mix}} \neq 0$, such as in the bcc and fcc HEAs composed of magnetic transition metals Mn, Co, Fe, Ni, and Cr, mixing of the elements is in principle not random (preferential local chemical environments are expected to form, at least in HEA samples that were thermally annealed at high temperatures), so the condition of "perfect" randomness fails. Geometric frustration is also not present in a lattice of bcc or fcc symmetry, so the formation of a SG phase in real HEAs with this kind of structure is questionable (and has not been reported in the literature so far). It can be expected that hexagonal HEAs based on different

combinations of RE elements from the lanthanide series with variable concentrations will constitute an inexhaustible source of alloys with rich (H,T) phase diagrams comprising conventional and exotic magnetically ordered and disordered phases.

(5) Our employed term of "random pinning potential" for a qualitative discussion is a kind of "emergency exit" in the lack of a proper microscopic model. The same term has been used by Nayak *et al.* [33] for the description of complex magnetism of intrinsically disordered Heusler compound Mn_2PtGa, where the phase diagram shows ferrimagnetic, AFM, and SG phases. The RKKY interaction is certainly the underlying interaction, but how should it be handled for such a highly chemically disordered system?

[1] J. W. Yeh, S. K. Chen, S. J. Lin, J. Y. Gan, T. S. Chin, T. T. Shun, C. H. Tsau, and S. Y. Chang, Adv. Eng. Mater. **6**, 299 (2004).

[2] J. W. Yeh, Ann. Chim. Sci. Mat. **31**, 633 (2006).

[3] See, for a review, Y. Zhang, T. T. Zuo, Z. Tang, M. C. Gao, K. A. Dahmen, P. K. Liaw, and Z. P. Lu, Prog. Mat. Sci. **61**, 1 (2014), and references therein.

[4] M. Feuerbacher, M. Heidelmann, and C. Thomas, Mat. Res. Lett. **3**, 1 (2014).

[5] A. Takeuchi, K. Amiya, T. Wada, K. Yubuta, and W. Zhang, JOM **66**, 1984 (2014).

[6] B. Cantor, I. T. H. Chang, P. Knight, and A. J. B. Vincent, Mater. Sci. Eng. A **375–377**, 213 (2004).

[7] R. A. Alberty and R. J. Silbey, *Physical Chemistry* (John Wiley & Sons, New York, 1992), p. 92.

[8] X. Yang and Y. Zhang, Mat. Chem. Phys. **132**, 233 (2012).

[9] O. N. Senkov, G. B. Wilks, D. B. Miracle, C. P. Chuang, and P. K. Liaw, Intermetallics **18**, 1758 (2010).

[10] O. N. Senkov, J. M. Scott, S. V. Senkova, D. B. Miracle, and C. F. Woodward, J. Alloys Compd. **509**, 6043 (2011).

[11] P. Koželj, S. Vrtnik, A. Jelen, S. Jazbec, Z. Jagličić, S. Maiti, M. Feuerbacher, W. Steurer, and J. Dolinšek, Phys. Rev. Lett. **113**, 107001 (2014).

[12] A. Takeuchi and A. Inoue, Mat. Trans. **46**, 2817 (2005).

[13] D. B. Miracle, J. D. Miller, O. N. Senkov, C. Woodward, M. D. Uchic, and J. Tiley, Entropy **16**, 494 (2014).

[14] L. Vegard, Z. Physik **5**, 17 (1921).

[15] See, for a review, J. Jensen and A. R. Mackintosh, *Rare Earth Magnetism* (Clarendon Press, Oxford, UK, 1991), and references therein.

[16] J. A. Mydosh, *Spin Glasses: An Experimental Introduction* (Taylor & Francis, London, 1993), p. 67.

[17] See, for a review, A. Tari, *The Specific Heat of Matter at Low Temperatures* (Imperial College Press, London, 2003), and references therein.

[18] *Ibid.*, Ref. [17] p. 249.

[19] K. Binder and A. P. Young, Rev. Mod. Phys. **58**, 801 (1986).

[20] R. J. Elliott and F. A. Wedgwood, Proc. Phys. Soc. **81**, 846 (1963).

[21] H. Miwa, Prog. Theor. Phys. **29**, 477 (1963).

[22] E. Segal and W. E. Wallace, *Rare Earth Intermetallics* (Academic Press, New York, 1973).

[23] R. W. Williams and A. R. Mackintosh, Phys. Rev. **168**, 679 (1968).

[24] W. C. Koehler, in *Magnetic Properties of Rare Earth Metals,* edited by R. J. Elliott (Plenum Press, London, 1972), p. 81.

[25] W. D. Corner and B. K. Tanner, J. Phys. C **9**, 627 (1976).

[26] M. T. Hutchings, Point charge calculations of energy levels of magnetic ions in crystalline electric fields, in *Solid State Physics*, edited by F. Seitz and D. Turnbull (Academic Press, New York, 1964), Vol. 16, p. 227.

[27] D. Sherrington and S. Kirkpatrick, Phys. Rev. Lett. **35**, 1792 (1975).

[28] G. Parisi, Phys. Rev. Lett. **50**, 1946 (1983).

[29] B. D. Gaulin, J. N. Reimers, T. E. Mason, J. E. Greedan, and Z. Tun, Phys. Rev. Lett. **69**, 3244 (1992).

[30] A. Lafond, A. Meerschaut, J. Rouxel, J. L. Tholence, and A. Sulpice, Phys. Rev. B **52**, 1112 (1995).

[31] P. Schiffer, A. P. Ramirez, D. A. Huse, P. L. Gammel, U. Yaron, D. J. Bishop, and A. J. Valentino, Phys. Rev. Lett. **74**, 2379 (1995).

[32] M. J. P. Gingras, C. V. Stager, N. P. Raju, B. D. Gaulin, and J. E. Greedan, Phys. Rev. Lett. **78**, 947 (1997).

[33] A. K. Nayak, M. Nicklas, S. Chadov, C. Shekhar, Y. Skourski, J. Winterlik, and C. Felser, Phys. Rev. Lett. **110**, 127204 (2013).